Applied Catalysis B: Environmental 297 (2021) 120398

Contents lists available at ScienceDirect

Applied Catalysis B: Environmental

journal homepage: www.elsevier.com/locate/apcatb

Discovering indium as hydrogen production booster for a Cu/SiO_2 catalyst in steam reforming of methanol

Filippo Bossola [a], Thantip Roongcharoen [b,1], Mauro Coduri [c], Claudio Evangelisti [b], Ferenc Somodi [d], Luca Sementa [e,1], Alessandro Fortunelli [b], Vladimiro Dal Santo [a,*]

[a] CNR-Istituto di Scienze e Tecnologie Chimiche "Giulio Natta", Via C. Golgi 19, 20133, Milano, Italy
[b] CNR-Istituto di Chimica dei Composti Organometallici, Via G. Moruzzi 1, 56124, Pisa, Italy
[c] Department of Chemistry, University of Pavia, Viale Taramelli 16, 27100, Pavia, Italy
[d] Centre for Energy Research, Surface Chemistry and Catalysis Department, PO Box 49, Budapest, H-1525, Hungary
[e] CNR-Istituto per i Processi Chimico-Fisici, Via G. Moruzzi 1, 56124, Pisa, Italy

ARTICLE INFO

Keywords:
Copper-indium
Hydrogen
Methanol steam reforming
Selectivity
Electronic properties

ABSTRACT

We report on the use of In as an effective H_2 production promoter in a Cu/SiO_2 catalyst for the steam reforming of methanol. To date, In promotion has been limited to noble metals because of its tendency to "bury" other metals thus compromising the catalytic activity. Here, we prepared a silica-supported Cu-In catalyst via a urea-assisted co-precipitation method that showed a higher H_2 productivity compared to the monometallic catalyst and a remarkable H_2/CO_2 molar ratio of almost 3 at 220 °C. Through XPS, XRPD and HRTEM-EDX along with H_2- and CO-TPR, H_2O-TPD, and N_2O titrations, supported by computational modeling, we attributed such superior performances to an easier H_2O activation due to improved electronic properties of the Cu phase, that is, its lower oxidation state via electron density transfer from the InO_x buffer phase as a 1D "necklace" structures crucially mediating the interaction of small Cu nanoparticles (2.6 nm) and silica.

1. Introduction

In-based catalysts have been known for quite some time [1–3] and have found a renewed interest as 100 % selective catalysts for the methanol synthesis from syngas [4]. In the "reverse" reaction, that is the methanol steam reforming (MSR), InO_x itself is active as a catalyst, but the H_2 production rates are generally low [3,5,6]. For this reason, In is supported on high surface area oxides, such as Al_2O_3 [7,8], often in combination with more active metals, such as Pt [7,9,10] or Pd [11–13].

The most relevant contribution of In to the MSR reaction is the improvement of the H_2 and CO_2 selectivity, with CO suppression reported at temperatures as high as 400 °C [5,13]. However, the only bimetallic In catalysts that has demonstrated thus far higher H_2 production rates over the monometallic counterparts is the $Pt/In_2O_3/Al_2O_3$ catalyst reported by Men and co-workers [12]. They ascribed the improved H_2 production to the proximity, or even partial coverage, of oxidized In to Pt nanoparticles that facilitates the H_2O activation. Interestingly, no significant improvement in the methanol conversion was reported by the authors. With Pd-based catalysts, In forms alloys and promotes long-term stability [13]. A surface enrichment of In was reported during the course of the reaction which, depending on the reaction conditions, can cause a total loss of activity due to severe coverage of the Pd nanoparticles.

From these studies, it can be drawn that the M-In interaction upon reductive treatment is crucial and is highly influenced by the M/In ratio and the reaction/pre-treatment conditions [14]. Despite the nearly CO-free H_2 streams obtained, the high cost of Pt and Pd is an important penalty towards the development of M-In bimetallic catalysts for sustainable H_2 production.

An alternative catalytic element is Cu, the benchmark metal for the MSR reaction [15–17] Matsumura et al. [18] tested a series of Cu-In catalysts at different In loadings reporting however a dramatic loss of activity caused by the InO_x phase covering the Cu nanoparticles. A similar phenomenon partially happens with Pd [13], but in the case of Cu even In loadings as low as 2–5 wt.% suppress the H_2 productivity [18]. Interestingly, in the work by Matsumura et al. [18] it was evidenced that the activity of a $Cu/ZnO/ZrO_2$ catalyst is greatly stabilized by In at high temperatures. The preparation procedure reported in that

* Corresponding author.
E-mail address: vladimiro.dalsanto@cnr.it (V. Dal Santo).
[1] Equally contributing authors.

https://doi.org/10.1016/j.apcatb.2021.120398
Received 1 April 2021; Received in revised form 24 May 2021; Accepted 28 May 2021
Available online 1 June 2021

work consists in a co-precipitation of all the three components, with a Cu loading of 50 wt.%, whereas Pt and Pd catalysts were prepared by impregnation of In salts on monometallic catalysts [7–9,12].

Neuman et al. [13] pointed out that the pretreatment conditions determine the final state of the bimetallic In catalyst, and in particular of the metal-In interaction. The use of relatively low temperature (300 °C) for the reduction treatments in H_2 seems to preserve the structural integrity of the main metal nanoparticles while avoiding excessive In coverage.

In the light of the promising results by Matsumura et al. [18], but aiming at an increased H_2 productivity analogous to that reported by Liu et al. [7,8], and being aware of the encapsulating action of In on metallic nanoparticles [13], in this work we devise and report a bimetallic Cu-In catalyst in which the presence of In not only does not compromise the exposure of Cu but in fact promotes H_2 productivity. Since the MSR activity is strongly affected by the catalyst support [8,19], especially when Cu is involved [20–22], to single out the promotional effect of In disentangled from other phenomena, we chose silica as a support because it is known to be inert during the reforming reactions with methanol [23,24]. Our major achievement in the present study is first of all to show that the promotional effect of In is not limited to the stabilization of Cu [18], but, rather, if combined with a proper catalyst preparation method, In doping can act as H_2 production booster for Cu-based catalysts in the MSR reaction. We also provide a rationale for this achievement based on an exhaustive characterization and theoretical modeling.

2. Experimental

2.1. Catalyst preparation

The catalysts were prepared via a urea precipitation [25]. Urea (2.55 *g*) was dissolved in ultrapure H_2O at room temperature in a 250 mL three-necked round bottom flask. Then silica (1.5 *g*, Davisil, grade 645, 60–100 mesh, 150 angstroms, Sigma Aldrich) was suspended in the solution under continuous stirring. This was followed by the addition of the appropriate amount of the precursor solutions in order to reach the desired metal content: 0.06 M $InCl_3$ and 0.2 M $Cu(NO_3)_2$ solutions were used. The total reaction volume was 160 mL in each case. The flask was equipped with a H_2O condenser and the mixture was then heated up to 90 °C with a heating mantle equipped with a temperature controller using 5 °C/min heating rate. The temperature was held for 3 h. Afterwards, the heating mantle was removed, and the mixture was cooled down to room temperature with a H_2O bath. The catalyst suspension was centrifuged and re-suspended three-times in 80 mL ultrapure H_2O, then dried in an oven overnight at 80 °C. In all the catalysts the nominal Cu content is 15 wt.%, while the In is nominally 1 wt.% or 5 wt.%. For instance, the Cu-1In/SiO_2 catalyst features Cu at the 15 wt.% and In at the 1 wt.%.

2.2. Catalyst characterization

The total Cu content was determined by Inductively Coupled Plasma Optical-Emission Spectroscopy (ICP-OES) (ICAP6300) after digestion in aqua regia.

The BET specific surface area and the BJH pore width and volume were determined by nitrogen physisorption isotherms at 77 K with a ASAP2020 apparatus. Prior to each analysis, the samples were degassed for 3 h at 110 °C in high vacuum.

Both temperature programmed reduction in H_2 flow (H_2-TPR) and N_2O titrations were performed using a Micromeritics PulseChemisorb 2700. An 8 vol.% H_2/Ar mixture was used as analysis gas. 15 mg of samples diluted with 300 mg of silica sand were loaded in a U-shaped quartz reactor. Simple H_2-TPR analyses were carried out by ramping up the temperature at 8 °C/min until about 500 °C, while for those used in the N_2O titrations the temperature was set to 300 °C and held for 30 min. After the first H_2-TPR, the reactor was cooled to 60 °C under 30 mL/min Ar flow. Then, 20 vol.% N_2O was allowed to flow for 5 min at 80 mL/min. Finally, the reactor was purged from the N_2O by flowing Ar at the same temperature for one hour and a second H_2-TPR was performed. The exposed Cu was calculated using the following equation [26]:

$$S_{Cu} = \frac{2A_1 N_a}{100\ (A_2)(AM_{Cu})(1.4 * 10^{19})} Cu_{tot}$$

S_{Cu} is the exposed surface Cu (m^2_{Cu}/g_{cat}), N_a is the Avogadro number (atoms/mol), AM_{Cu} is the atomic mass (g/mol), $1.4 * 10^{19}$ is the surface Cu packing density (atoms/m^2), and Cu_{tot} is the Cu loading (%). A_1 and A_2 are the peak areas of the first and the second reduction, respectively.

CO temperature programmed reduction (CO-TPR) analyses, as well as H_2O and CH_3OH temperature programmed desorption analyses (H_2O-TPD and CH_3OH-TPD, respectively), were performed by using a home-made gas rig, described elsewhere [27], connected downstream to a mass spectrometer (Hiden Analytical, HPR20). In all cases, 50 mg of the samples were used for the analyses. As for the CO-TPR, before reduction with 20 mL/min of 50 vol.% CO/Ar and a ramp rate of 8 °C/min, the samples were treated with 30 mL/min He flow at 130 °C for 1 h. In the case of the TPD analyses, the samples were first reduced with a 15 mL/min H_2 flow for 30 min at 300 °C and a ramp of 10 °C/min; then, after purging with He flow (20 mL/min) for 30 min at the same temperature, the samples were cooled to 70 °C. At this point, the samples were saturated with H_2O or CH_3OH vapors by flowing the carrier gas through a saturator at 25 °C and purged again with He (20 mL/min). Finally, the desorption was carried out by ramping up the temperature at 8 °C/min under the same He flow starting from 50 °C.

Transmission electron microscopy (TEM) micrographs were collected with a ZEISS LIBRA200FE microscope with a 200 kV FEG source. Energy-dispersive X-ray spectroscopy (EDS – Oxford INCA Energy TEM 200) and elemental mapping were taken along with HAADF-STEM (high angular annular dark field scanning electron microscopy) images.

XRD patterns were collected on a Bruker d8 Advance diffractometer in Bragg-Brentano geometry equipped with a Ni-filtered Cu-Kα radiation. Preliminary data collection was performed at atmospheric condition from 10° to 50° 2θ, 0.05° step, and total 8 h acquisition.

As to the reduced samples, they were preserved in Ar atmosphere in a glove box and then mounted on an air-tight sample holder. To maximize the counting statistics before oxygen uptake, some fast scans were performed in the 35−55° 2θ range (step 0.1°, 18 min) to ascertain the presence of Cu rather than CuO or other alloys, and to extract the crystal size out of the peak broadening based on the Scherrer formula. In addition, a longer scan about 10 h long was carried out from 10 to 60° (step 0.05°). Peak broadening was extracted through single-peak fitting performed by the WinPLOTR software [28]. The reference patterns in Fig. 3 were simulated using GSAS software. The patterns were simulated based on the Cu structural model (F m −3 m, Cu in special position). The peak profile was computed considering Caglioti formula for instrumental resolution, taken with a LaB6 NIST standard, adding a Lorentzian contribution (LX in GSAS) related the isotropic finite size broadening. The LX value for each crystal size D was calculated based following equation, according to the GSAS user manual:

$$LX = \frac{18000\ K\ \lambda}{\pi\ D}$$

where K is Scherrer constant, λ the wavelength, LX the Lorentzian broadening parameter related to finite size.

For the determination of surface composition and oxidation state of the metals, X-ray photoelectron spectroscopy (XPS) measurements were done using a KRATOS XSAM 800 XPS machine equipped with an atmospheric pretreatment chamber. Al Kα characteristic X-ray line, 40 eV pass energy and FAT mode were applied for recording the XPS lines of Cu 2p, Cu LMM, In 3d, and Si 2p regions. Si 2p binding energy at 103.5

eV was used as reference for charge compensation. Although there is no single fundamentally correct method for precise correction of peak positions of insulating samples, the signal of adventitious carbon was used as an inner reference. The shift in the position of C 1s peaks after heat treatments was in between the acceptable range, that is, 284.8 +/− 0.3 eV (see Table S3). Therefore, the observed binding energy (B.E.) shifts larger than 0.3 eV can be accepted as real shift of the peak. For quantification of the XPS data, the measured raw peak areas of the elements were divided by the corresponding sensitivity factors. The samples were measured after the preparation, after reduction like that employed for the TPR measurements (an atmospheric pretreatment chamber connected to the UHV chamber with a load lock gate avoided exposing the samples to the air), and, finally, after re-oxidation in the air at room temperature.

2.3. Catalytic tests

A home-made fixed-bed (9 mm internal diameter) test unit was used to perform the catalytic tests [29] with 200 mg of catalyst (45-35 mesh) and a CH_3OH/H_2O solution at a steam-to-carbon (S/C) ratio of 1.3 (mol/mol). The carrier gas was He at atmospheric pressure. Before each run, the catalysts were reduced at 300 °C for 30 min with pure H_2 (15 mL/min). The gaseous products were analyzed with an on-line GC-TCD (Agilent 6890N). To better evaluate the activity of the Cu active sites, catalytic runs were carried out by varying the feed flow rate, but without altering the composition of the inlet mixture. Normalized contact times were calculated as the actual Cu exposed divided by the molar flow rate of methanol per second. The H_2 productivity is reported as mmol of H_2 produced per hour per gram of catalyst, while the selectivity was calculated by dividing the molar flow rate of H_2 by the sum of the molar flows of the products multiplied by the reforming factor of 3. CO, CO_2, and CH_4 selectivity was determined over the sum of the flow rates of the gaseous carbon-containing products. Turnover frequency (TOF) was calculated as rate of carbon moles converted (mmol/s * kg_{cat}) at the same conversion level over the Cu dispersion.

2.4. Computational details

The morphology of supported clusters suitable for simulating reactivity was obtained via a Global Optimization stochastic search. Global Optimization runs were performed based on the Basin-Hopping algorithm (BH) [30] coded in an in-house python code. Starting from a given initial atomic configuration, the algorithm randomly perturbs the coordinates followed by a local geometry optimization to obtain a new configuration that is accepted or rejected according to the Metropolis criterion [31], i.e., the new configuration is accepted as the starting configuration for the next BH step if its energy (E_f) is lower than the initial one (E_i) or if the Metropolis criterion "$\exp[-(E_f - E_i)/k_B T_{GO}] > r$" is satisfied, where r is a random number, k_B is the Boltmann constant, and T_{GO} is a fictitious temperature. The algorithm then iterates the previous steps by starting from the current accepted configuration. Each BH run generated about 1200 configurations, with an acceptance rate determined by a fictitious temperature T_{GO} of 2000 K.

We performed multiple BH runs to explore the density-functional theory (DFT) Potential Energy Surfaces (PES) of three different stoichiometric clusters, both bare and supported on the (001) facet of silica, SiO_2, with stoichiometry: $Cu_{38}O_8$, $Cu_{38}In_4O_{10}$ and $Cu_{38}In_4O_{12}$. The (001) SiO_2 surface, exposing unsaturated oxygens with one dangling bond, was partially hydroxylated as presumably in experiment. The SiO_2 support was modeled with a slab made of six atomic layers non-stoichiometric and asymmetric with a unit cell with edge lengths of 1.99 nm and 1.72 nm. Unsaturated Si atoms exposed by the slab's bottom layer were capped with H atoms and kept frozen during the BH runs. On the topmost-layer side, 60 % of the protruding oxygens were terminated by H atoms to leave a region for the direct interaction of the cluster and the silica surface.

To accelerate as much as possible the cpu-demanding BH procedure, the DFT local optimizations were performed using the OPENMX code [32] that reduces the ab-initio computational burden by employing small-size optimal numerical basis sets [33], generated for describing the electronic configurations of atoms in a confining potential. The associated computational effort was further limited by describing core electrons with the aid of pseudopotentials, which also reduces the number of plane-waves needed for solving the Poisson equation by the OPENMX-proprietary FFT algorithm [34]. Finally, the Kohn Sham equations based on the Perdew-Burke-Ernzerhof (PBE) exchange-correlation functional [35] were solved by employing 'Quick' type basis sets available from the PAO2019 database [36], PBE19 norm-conserving pseudopotentials [36] and a plane-wave cutoff of 150 Ry.

On the structures of the deposited catalyst clusters produced by the GO approach, further calculations were performed to predict H_2O adsorption, H_2O dissociation, and core-level shifts (CLS), based on density-functional theory (DFT) using the Quantum ESPRESSO (QE) package [37,38]. GBRV's ultra-soft pseudopotentials [39] along with the Perdew-Burke-Ernzerhof (PBE) exchange-correlation functional were employed to calculate the energetics [35]. A plane-wave basis set with a cut-off energy of 40 Ry was used for the expansion of the wave functions, while a cutoff of 200 Ry was used for expanding the charge density. Spin-polarized calculations were always conducted, although the systems here investigated were almost exclusively closed-shell. In the QE structural optimizations and barrier evaluation, only the bottom layer of the silica (SiO_2) support was kept frozen, whereas the second layer of SiO_2, and all atoms of pure Cu and bimetallic Cu-In catalysts were fully relaxed without any constraints. The convergence energy threshold for the self-consistent-field (SCF) was set to 1×10^{-6} Ry. Calculations were performed at the Gamma point in the Brillouin zone of the unit cell.

The adsorption energy (ΔE_{ads}) was calculated as:

$$\Delta E_{ads} = E_{total} - E_{cat} - E_{H2O}$$

where E_{total}, E_{cat}, and E_{H2O} correspond to the total energy of the complex with H_2O adsorption, the total energy of the catalyst without H_2O, and the total energy of the H_2O molecule, respectively. More negative values of ΔE_{ads} indicate stronger binding.

In order to attain the minimum energy pathways (MEP) for H_2O dissociation, NEB and climbing image NEB methods [40,41] were adopted to search for the transition state (TS) of each elementary step. To locate each transition state rapidly and accurately, NEB calculation was performed to find approximate structure of transition state by using five intermediate images between the initial and final states. Then these five optimized intermediate structures were included as the initial inputs for second NEB in which ten intermediate images were generated and optimized to acquire minimum energy reaction paths and possible transition states. Based on ten intermediates obtained from second NEB, final transition state structure was accurately located by NEB climbing-image with the force convergence of 0.1 eV/Å. The energy barrier (E_a) was determined as:

$$E_a = E_{TS} - E_{IS}$$

where E_{TS}, E_{IS} represent the total energy of the transition state and its preceding initial state. Atomic charge and electrons transfer were evaluated based on the Löwdin population analysis [42].

The core-level shifts (CLS) of Cu-2p and In-3d states were calculated using a spin-averaged pseudopotential approach [43], which requires the generation of pseudopotentials with a specific core-hole and to evaluate the pseudopotential energy difference between the system's ground state and the system containing one excited atom. Excited effective-potentials were generated within the Projector-Augmented Wave (PAW) framework by starting from the PAW files available for both Cu and In within the GRBV dataset [39].

3. Results

3.1. Catalytic performances

The catalysts without Cu did not show any catalytic activity, as well as Cu/In_2O_3. The activity of the Cu-5In/SiO_2 catalyst was very low, with 1 % conversion at 260 °C (not shown). The catalytic evaluation results of Cu/SiO_2 and Cu-1In/SiO_2 are listed in detail in Tables S1 and S2. To note that rather than using the sheer values of H_2 selectivity, which in our opinion do not provide the best picture of the outcome of the reaction, we will use the H_2/CO_2 molar ratio.

The Cu/SiO_2 catalyst showed a stable catalytic activity in line with previous reports [23,24,44,45] with a methanol conversion of 57.1 % after 17 h at 260 °C and normalized contact time of around 0.005 s. Under these conditions, CO selectivity was relatively low at 0.37 % (Table S1) and a H_2/CO_2 molar ratio of 2.76.

Quite interestingly, with the addition of In, such ratio rose to the almost stoichiometric value of 2.99, that corresponds to 100 % H_2 selectivity (Fig. 1a, Table S2), accompanied by a drop in CO selectivity to values as low as 0.07 % (Table S2). This imply that, per almost each mole of CO_2, no other products were formed other than H_2. Cu-1In/SiO_2 maintained a general improvement in H_2 productivity and H_2/CO_2 ratio over Cu/SiO_2 throughout all the range of temperatures examined, that is, between 150 °C and 300 °C (Fig. 1b and Tables S1 and S2). The latter catalyst did not reach a comparable H_2/CO_2 ratio and H_2 productivity even at 300 °C of reaction temperature.

As for the H_2 productivity values, the Cu/SiO_2 catalyst showed about 237 mmol/h * g_{cat}, that is lower compared to other Cu-based catalysts [16,21], but in presence of 1 wt.% of In the productivity was about 301 mmol/h * g_{cat} at 260 °C.

The influence of the contact time calculated over the Cu exposed on H_2 production rate was examined between around 0.005 s and 0.015 s by adjusting the feed rate of the carrier and CH_3OH/H_2O solution to keep the composition constant (Fig. 1c). In the whole range examined, the Cu-1In/SiO_2 catalyst showed a higher H_2 productivity, and, at the lowest normalized contact time, it showed a H_2/CO_2 ratio of 2.69, a markedly higher value than the 2.01 of the Cu/SiO_2 catalyst.

These results demonstrate that the Cu-1In/SiO_2 catalyst outperforms Cu/SiO_2 in terms of both H_2 productivity and H_2/CO_2 ratio. The higher TOF, calculated at the same conversion level of about 40 %, of Cu-1In/SiO_2 (24×10^3 s^{-1}) with respect to Cu/SiO_2 (19×10^3 s^{-1}) is the ultimate proof of such superiority.

The relatively low CO production shown by our Cu/SiO_2 catalyst could be due to high Cu dispersion, like in the case of the Cu-MCM41 catalysts described by Deshmane et al. [46]. CH_3OH-TPD analyses (Fig. S1) evidenced that only the Cu-1In/SiO_2 catalyst did not produce any CO during the desorption, which is in line with previous reports [5, 13]. In addition, the same catalyst generated more CO_2 than all the other ones, thus corroborating the remarkable H_2/CO_2 ratio found during the catalytic tests. As for the lack of activity of the Cu/In_2O_3 and Cu-5In/SiO_2 catalysts, that could be due to an almost null adsorption of methanol for the former, and delayed desorption of methanol, which started at temperature far above (about 350 °C) those used in this work, for the latter. Since the silica support is inert in MSR [23,24] reactions, and both the In/SiO_2 catalysts and the Cu/In_2O_3 catalyst did not display any relevant catalytic activity, the H_2 promotion must be the result of some synergy between Cu and In when "dosed" at the right ratio on the silica. The fact that the H_2 productivity with Cu-1In/SiO_2 was higher compared to the Cu/SiO_2 catalyst at all the normalized contact times further supports this hypothesis.

To better understand how and in what extent this synergy occurs, a series of characterizations tools were used to investigate the morphology as well as the redox and electronic properties of the catalysts.

3.2. Morphology

The textural characteristics of the catalysts are listed in Table 1, while the N_2 physisorption isotherms and the pore distributions are reported in Fig. S2. The Cu/In_2O_3 sample showed the lowest surface area (7 m^2/g) and the lowest pore volume (0.07 cm^3/g). The two samples containing only In featured practically the same morphological characteristics with about 260 m^2/g and 1.23 cm^3/g of surface area and pore volume, respectively. Starting from Cu/SiO_2, the addition of In caused a decrease in both surface area and pore volume. Nonetheless, both the bimetallic catalysts exhibited a surface area larger than 200 m^2/g and a pore volume of 0.82–0.88 cm^3/g which, as anticipated, excludes a major role of the silica support in the higher performances of Cu-1In/SiO_2 catalyst.

STEM-EDX maps (Fig. 2) of Cu-1In/SiO_2 showed that both Cu and In are homogeneously dispersed all over the surface of the catalyst with the signals of Cu and In perfectly overlapping. No relevant segregation of InO_x was revealed. Such a proximity might hint to the formation of Cu-In mixed phases or even alloys, as for instance reported with Pd [12,13]. The phase composition was then investigated by XRD.

The as prepared catalysts were fully amorphous irrespective of the In content (Fig. S3), so patterns were collected after reduction at 300 °C in H_2 flow for 30 min to mimic the activation step prior to the catalytic runs. As detailed in the experimental section, the catalysts were

Table 1
Catalysts BET surface areas and pore volumes.

Entry	BET surface area (m^2/g)	Pore volume (cm^3/g)
1In/SiO_2	264	1.23
5In/SiO_2	260	1.21
Cu/In_2O_3	7	0.07
Cu/SiO_2	352	0.95
Cu-1In/SiO_2	239	0.82
Cu-5In/SiO_2	215	0.88

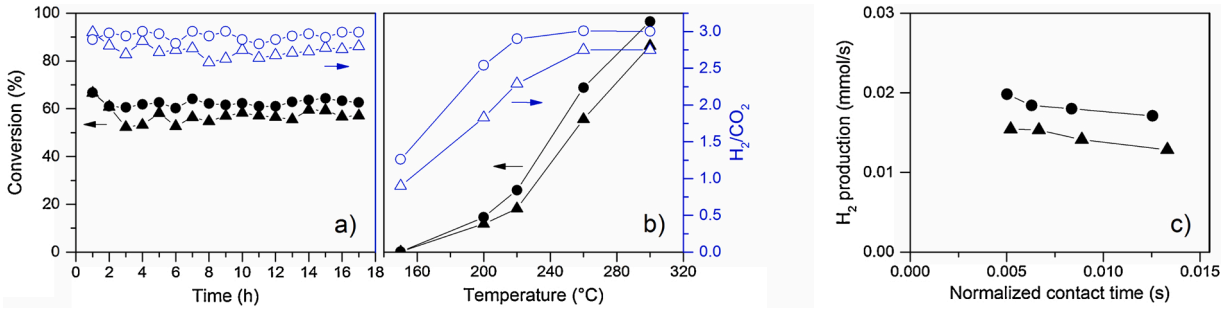

Fig. 1. Catalytic activity of Cu/SiO_2 (triangles) and Cu-1In/SiO_2 (circle): a) Stability test carried out at 260 °C and at a normalized contact time of 0.005 s^{-1}; b) Effect of the temperature on the activity between 150 °C and 300 °C at a normalized contact time of 0.005 s^{-1}; c) Effect of the normalized contact time on the H_2 production rate evaluated at 260 °C. A S/C molar ratio of 1.3 was used in all the tests.

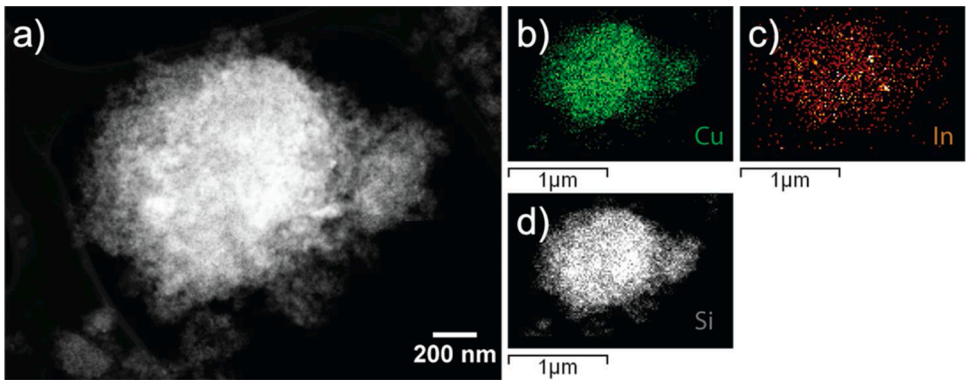

Fig. 2. STEM measurements of Cu-1In/SiO_2: a) HAADF image of a catalyst grain; b-d) STEM-EDX mapping of the catalyst showing the Cu and In dispersion present in the catalyst: b) Cu map (green), c) In map (red) and d) Si map (grey) (For interpretation of the references to colour in this figure legend, the reader is referred to the web version of this article.).

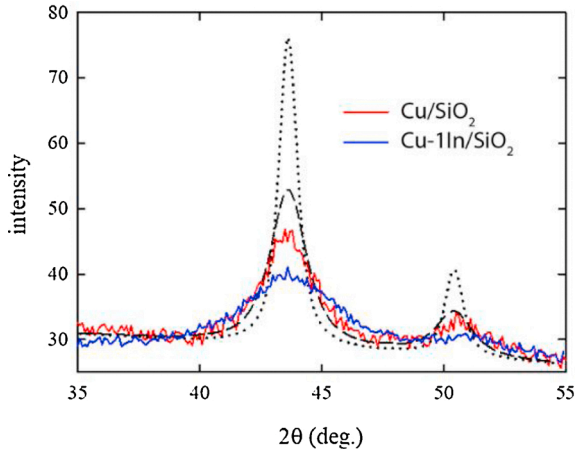

Fig. 3. Experimental XRD patterns of Cu/SiO_2 (red) and Cu-1In/SiO_2 (blue) collected under reducing atmosphere within an air-tight sample holder in the 35° to 55° 2θ range. Simulated patterns for Cu nanoparticles (black) with 5 and 10 nm crystal size are shown in dashed and dotted lines, respectively (For interpretation of the references to colour in this figure legend, the reader is referred to the web version of this article.).

investigated maintaining the reducing atmosphere by means of an airtight sample holder. Since the catalysts were found to be mostly amorphous, and the oxidation occurred within few hours notwithstanding the container, fast diffraction patterns were collected in a diffraction range where the main Cu (or possibly CuIn) and CuO diffraction peaks occur. This allowed to optimize the counting statistics related to the active Cu compound. Fig. 3 shows the sum of the fast diffraction patterns for Cu-1In/SiO_2 and Cu/SiO_2 as red and blue solid lines, respectively. The noise comes from the Ar atmosphere that attenuates the beam and from the low crystallinity. The experimental patterns are centered very close to the main (111) reflection of metallic Cu. No apparent shift of the peak position, that could indicate Cu alloying, is observed with the addition of In. Moreover, long patterns collected at ambient conditions revealed the crystallization of CuO only, thus ruling out the presence of other secondary phases.

The crystallite size was estimated to be about 4 and 2.5 nm for Cu/SiO_2 and Cu-1In/SiO_2, respectively (Table 2). Anyhow, even though noise can affect the correct estimation of the crystallite size, it is evident that crystallite dimensions are well below 5–10 nm. To prove that, patterns corresponding to crystals with 5 and 10 nm were simulated and plotted in Fig. 3 as dashed and dotted lines, respectively. Keeping in mind the limitations of the Scherrer approach, we can safely state that Cu crystallites size is well below 10 nm and that no increase in crystal size is induced by the addition of In.

Table 2
Cu loadings, percentage of Cu reduced after H_2-TPR until 300 °C, exposed Cu, and Cu crystalline sizes of the catalysts.

Entry	Cu loading[a] (wt.%)	Cu reduced[b] (%)	Exposed Cu[c] (m^2_{Cu}/g_{cat})	Cu crystallite size (nm)	
				XRPD	HRTEM
Cu/In_2O_3	15.3	93.9	7.1[b]	*N.D.*[d]	*N.D.*
Cu/SiO_2	12.9	78.8	75.8	4.0	4.2
Cu-1In/SiO_2	13.7	84.8	56.4	2.5	2.6
Cu-5In/SiO_2	12.1	20.0	6.4	*N.D.*	*N.D.*

[a] Determined by ICP-OES.

[b] After H_2-TPR.

[c] Determined by N_2O titration.

[d] Not determined.

HRTEM images were used to validate the XRD data and calculate the particles size distributions in the catalysts. Before taking the HRTEM pictures, the catalysts were reduced as for the XRD analyses. In good accordance with XRD evidence, the Cu nanoparticles in the Cu-1In/SiO_2 catalyst are smaller than those in the monometallic catalyst, with sizes centered at 2.6 nm and 4.2 nm, respectively. The smaller size of the nanoparticles in Cu-1In/SiO_2 and their stability after 17 h of reaction (Figs. 1b and 4b) might suggest this as the reason behind the superior performances of the doped catalysts because of a higher amount of active Cu exposed. However, a more efficient use of the catalyst by itself would not account for the improved H_2 productivity at the same normalized contact time (Fig. 1c). Other factors other than the morphology and the Cu nanoparticle size must be critically affecting the catalytic system.

3.3. Catalysts reducibility and Cu exposure

TPR analyses with H_2 and CO were performed to assess the reducibility of the catalysts (Fig. 5), while the exposed Cu was determined by N_2O titrations (Table 2).

No major reduction peaks were observed during the H_2-TPR analyses of 1In/SiO_2 and 5In/SiO_2 before 300 °C, and the very weak features at higher temperatures are likely due to the reduction of InO_x finely dispersed on the surface of the silica support [1] (Fig. 5a). Hence, any reduction features displayed by the Cu catalysts below 300 °C are to be ascribed solely to the reduction of Cu, while intermetallic compounds or alloys are reported to form at temperatures around 450 °C [47]. The

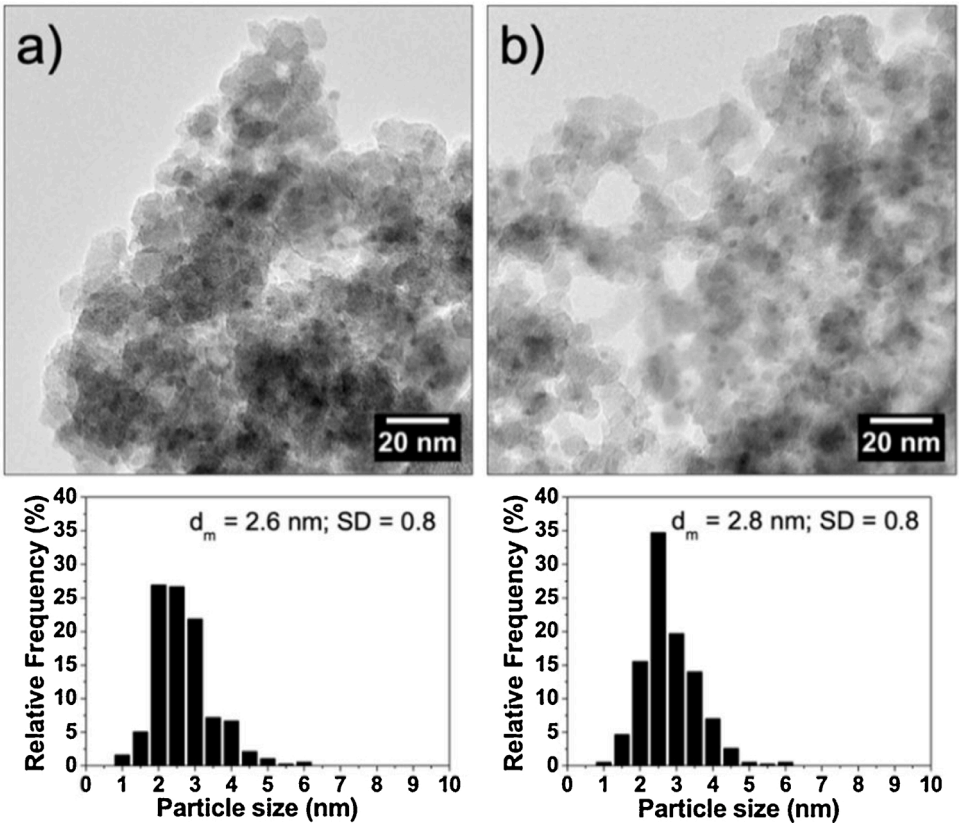

Fig. 4. Representative TEM micrograph and particles size distribution of Cu-1In/SiO_2: a) reduced and b) after reaction (20 h time-on-stream and temperature = 260 °C).

presence of just one reduction peak in the profile of the Cu/In_2O_3 catalyst at 227 °C, which corresponds to a degree of reduction of the Cu of 93.9 %, indicates that most of the Cu is reduced with the pretreatment before the reaction (Fig. 5a). However, the N_2O titration revealed that only a limited amount of Cu is exposed (7.1 m^2_{Cu}/g_{cat}), which might be due to InO_x covering of the Cu phase upon reduction [13]. The Cu/SiO_2 catalyst had also just one reduction peak, but at a slightly higher temperature of 239 °C. Even though the reduction degree is only 78.8 %, the exposure of metallic Cu is one order of magnitude higher than the Cu/In_2O_3 catalyst with 75.8 m^2_{Cu}/g_{cat} exposed. These values are not unexpected as silica is well-known to be a support on which Cu can be easily dispersed or even lost within [46,48–50]. Interestingly, in the presence of 1 wt.% of In, a quite similar reduction profile was observed at the same temperature of Cu/SiO_2, but its area indicates a higher H_2 consumption and in turn a higher reduction degree (84.8 %). The Cu exposed in Cu-1In/SiO_2 was however only 56.4 m^2_{Cu}/g_{cat}. The Cu-5In/SiO_2 catalyst is markedly different with one weak reduction peak at 256 °C and a second one at about 370 °C. The exposed Cu is very low, like for the Cu/In_2O_3 catalyst.

It is clear that the presence of In influences the reduction of the Cu. However, the analyses performed with H_2 on the Cu/SiO_2 and Cu-1In/SiO_2 catalysts differed only in the intensity of the reduction peak without providing much more information. So, to get more insights on the presence of any hard-to-reduce species, CO-TPR analyses were performed since CO is more efficient in Cu oxide reduction than H_2 [51]. The reduction profiles obtained with CO (Fig. 5b) are indeed more complicated than the H_2-TPR profiles. Bear in mind that the peaks above 300 °C are due to the Boudouard reaction catalyzed by metallic Cu [52].

The high reducibility of Cu/In_2O_3 is again confirmed by this analysis with two very sharp peaks at low temperature (175 °C and 193 °C), whereas the reduction of Cu-5In/SiO_2 started later and peaked at 260 °C. Both Cu/SiO_2 and Cu-1In/SiO_2 catalysts showed a reduction peak centered around 195 °C which can be ascribed to the reduction of finely dispersed CuO to metallic Cu [53]. Just like the H_2-TPR profiles, Cu-1In/SiO_2 exhibited a more intense peak compared to Cu/SiO_2, further confirming that In facilitates the reduction of Cu. Interestingly, at a temperature around 290 °C, a broad feature is visible in the profile of Cu/SiO_2, which can indicate the presence of Cu species that are difficult to reduce possibly because strongly interacting with the silica support. No such feature was observed in the Cu-1In/SiO_2 reduction profile.

Whereas with 5 wt.% of In the reduction of Cu is strongly impaired due to severe covering of the Cu by the In, the TPR analyses clearly indicate that 1 wt.% of highly dispersed In favors the reduction of Cu and prevents the formation of Cu species that are difficult to reduce. But again, more Cu in the reduced form cannot explain the higher H_2 productivity at all normalized contact times (Fig. 1c) and the higher TOF (see section 3.1) of the Cu-1In/SiO_2 catalyst.

3.4. Electronic structure

XPS spectra were collected before and after reduction *in-situ* with H_2 at 300 °C as well as after room temperature re-oxidation of the reduced samples (Figs. S4–S6). All the data for all the catalysts are listed in Table S3, while the surface composition of the catalysts is summarized in Table 3.

No shake up peaks were found in any of the Cu 2p spectra of the H_2-treated catalysts, thus indicating a complete reduction of the surface Cu. The absence of shake up peaks implies that unreduced Cu in the Cu/SiO_2 and Cu-1In/SiO_2 catalysts (see Table 2) is not on the surface but rather hidden into the support and/or the InO_x phase. Auger parameters were around 1851.0 eV for all the catalysts examined [54]. It was shown that the calculated Auger parameter significantly decreased with Cu particle size below 25 Å on insulating support materials [55]. Since the

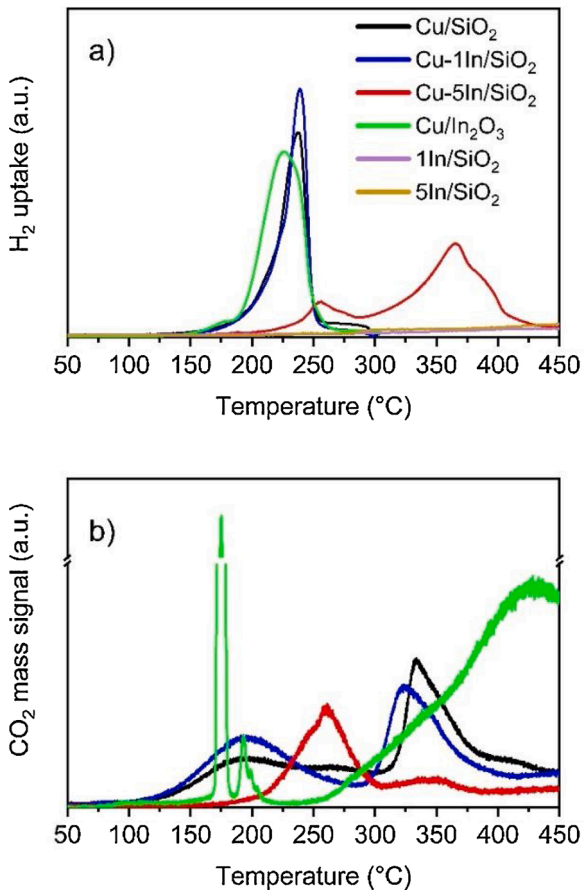

Fig. 5. a) H_2-TPR and b) CO-TPR profiles (For interpretation of the references to colour in this figure legend, the reader is referred to the web version of this article.).

average particle size in the present study was larger than 25 Å, the value of the Auger parameter calculated above shows the presence of metallic Cu on the catalyst surface. Cu^+ sites from possible incomplete reduction remained undetected by XPS measurements.

The surface Cu/Si and Cu/In atomic ratios, before and after the reduction, support what was inferred with the TPR analyses and N_2O titrations about the InO_x encapsulating the Cu and, consequently, its exposure. Among the as prepared catalysts, Cu-5In/SiO_2 showed the lowest Cu/Si and Cu/In atomic ratios, meaning that already after the preparation of the catalysts few Cu is available for reduction on the surface. After reduction, both ratios drop, further indicating that excessive In is detrimental to the exposure of the Cu phase. The fact that the few In in the Cu-1In/SiO_2 catalyst does not compromise the exposure of Cu can be verified by the very similar Cu/Si atomic ratio to the Cu/SiO_2 catalyst of about 0.11 (at/at) after reduction.

As for the position of the XPS peaks, which is influenced by the surface electron density [44,56], the Cu $2p_{3/2}$ peak of the Cu/SiO_2 after reduction is centered at 931.8 eV (Table S3), as expected for metallic Cu nanoparticles [44,51]. Similar binding energies were measured in the case of the In-containing catalysts: 931.7 eV and 931.5 eV for Cu-1In/-SiO_2 and Cu-5In/SiO_2, respectively. After room temperature oxidation of the reduced catalysts, the peaks shifted to higher binding energies indicating a re-oxidation of the surface of the catalysts. The In $3d_{5/2}$ peak position was the highest (445.3 eV for 1 wt% In and 444.9 eV for 5 wt% In) in the case of as prepared catalysts, whose surfaces are covered by the as deposited hydroxides. The peaks then shifted to lower binding energies (444.2 eV for 1 wt% In, 444.4 eV for 5 wt% In) in both In-containing samples after reduction. These B.E. values are attributed to the presence of non-stoichiometric InO_x on the surface on the basis of the previous TPR measurements (see Section 3.3), which showed that only partial reduction of In can be achieved after reduction at 300 °C [25], and because after room temperature exposure to the air these species re-oxidized as the +0.6 eV and +0.7 eV shift of the In 3d peaks indicate [57,58].

In did not form alloys with Cu after reduction, as ruled out by XRD and XPS (no B.E. shift of Cu 2p peaks in the presence of In). The close vicinity of InO_x phase to Cu nanoparticles, as shown by HRTEM (Fig. 2) and further supported by decreased N_2O adsorption (Table 2), could have nonetheless resulted in some interaction that would explain the higher selectivity of the Cu-1In/SiO_2 catalyst. The apparent progressive shift of the Cu $2p_{3/2}$ peak towards lower values, along with the concurrent increase of the In $3d_{5/2}$ peak position (Table S3), although alone cannot be a solid evidence, hint to some electron transfer occurring between the two. This hypothesis will be confirmed by our theoretical modeling in Section 3.5.

Liu et al. [7] reported that InO_x phase promotes the H_2 productivity of Pt catalysts by enhancing the H_2O activation. The same was observed with our Cu-1In/SiO_2 catalyst by performing H_2O-TPD (Fig. 6) analyses as it features a second peak at lower temperature compared to the profile of Cu/SiO_2. Such observation will be fundamental to the theoretical modeling (Section 3.5).

From the above overview, we suggest that the key is the higher surface electron density of the Cu nanoparticles. It is well reported that Cu catalysts supported on silica are far less performant than those supported on more reducible oxides [16]. The reason is the very poor activation of H_2O by the support [59], as also verified by us (Fig. 6), and because of the high metal-support interaction which hinders Cu reduction [23,60]. The magnitude of such a strong interaction could even cause the disappearance of Cu from the surface within few weeks from the preparation of the material [48]. Apart from this extreme situation, the electron density of metallic Cu nanoparticles supported on silica tends to be low, as evidenced by Cu $2p_{3/2}$ XPS peaks reported at values as high as around 933 eV [51,61]. But by deposition precipitation with urea as shown herein, a more reducible silica-supported catalyst can be prepared. To provide a comparison, even Cu nanoparticles supported on zirconia, which is known to stabilize the reduced state of Cu, have Cu $2p_{3/2}$ peaks at 932.0–932.1 eV [44,62]. Besides stabilizing the Cu nanoparticles (see Fig. 4), In or non-stoichiometric InO_x might act as an "electron buffer", which might increase the surface electron density of the Cu nanoparticles. In the next section the "buffer" role of InO_x will be investigated by the theoretical analyses.

The electronics of the metal nanoparticles are crucial for many reactions [47,63,64], including reforming reactions [65,66] and MSR with

Table 3
Surface composition of the Cu/SiO_2, Cu-1In/SiO_2, and Cu-5In/SiO_2 catalysts as prepared, after reduction, and after re-oxidation. Ratios are expressed as atom/atom.

	Cu/Si			Cu/In		
Entry	As prepared	Reduced	Oxidized[a]	As prepared	Reduced	Oxidized[a]
Cu/SiO_2	0.48	0.10	0.16	–	–	–
Cu-1In/SiO_2	0.36	0.11	0.21	29.46	20.84	25.97
Cu-5In/SiO_2	0.08	0.01	0.01	3.98	0.98	1.02

[a] In air at room temperature.

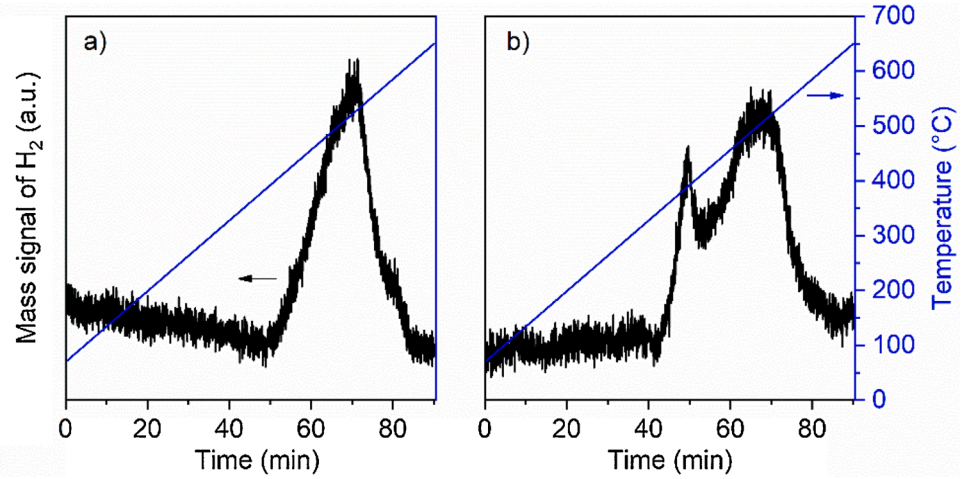

Fig. 6. H_2O-TPD analyses on a) Cu/SiO_2 and b) $Cu\text{-}1In/SiO_2$ catalysts performed after reducing the sample at 300 °C for 30 min under H_2 flow.

Cu-based catalysts [21,67,68]. In a recent publication by some of us [21], we described how small Cu nanoparticles in the range of 2–3 nm have poor electronic density on their surface but nonetheless are far more performant than bigger ones with typical electronic properties. We found that methanol preferentially adsorbs on the electron-poor Cu nanoparticles rather than on the support, thus speeding up the reaction. In the present work we adopted a different approach: The electron density of equally small Cu nanoparticles was increased by adding In obtaining again a higher H_2 productivity. Since such superior productivity is mostly due to an improved selectivity rather than to the methanol conversion, especially at high normalized contact times (see Fig. 1c), the enrichment of the electron density of the Cu nanoparticles is likely to favor the intermediates dehydrogenation and/or the formation of molecular H_2 [59].

3.5. Computational modeling

DFT modeling was conducted to better understand the origin of the enhanced H_2 production performance of the In-doped Cu catalyst.

Catalyst structural models at three different stoichiometry were first generated. Initially, reasonable starting geometries of a Cu cluster ($Cu_{38}O_8$) and two Cu-In clusters with a different oxygen content ($Cu_{38}In_4O_{10}$ and $Cu_{38}In_4O_{12}$) were derived in the gas-phase and then deposited on a partially hydroxylated SiO_2 (100) surface. The stoichiometry of these systems was chosen to model both un-doped ($Cu_{38}O_8$) and the experimentally-determined best-performing doped catalyst ($Cu\text{-}1In/SiO_2$), deriving two different models for the Cu-In system to allow for a more oxidized ($Cu_{38}In_4O_{12}$) or more reduced ($Cu_{38}In_4O_{10}$) state of the catalyst. In tune with the small size of the catalyst nanoparticles in experiment (2–4 nm in diameter) we use finite cluster models as close as possible to the experimental situation instead of the more common extended-facet models of the catayst. This allowed us to include in our model both finite-size effect and the role of the silica support. A number of atoms in the catalyst around 50 plus 122 atoms of the support entailed a computational effort affordable with our resources, although the final simulated size of the particle is around 1–1.5 nm in diameter and therefore smaller than in experiment. Then, a Global Optimization (GO) search [30] was performed for each cluster starting from random configurations and using 1200 Monte Carlo steps with shake moves as detailed in Section 2.4, thus obtaining the lowest-energy putative global minimum structures as depicted in Fig. 7 and reported in full in the SI.

The most important outcome of this GO structural search is that, despite the fact that the initial configurations of the Cu-In system had In atoms also on the top of the cluster far from the support, the GO search invariably produced a “necklace” or “belt” of partially oxidized In atoms (InO_x phase) at the interface with the silica support in the lowest-energy structures. The morphology of such “necklace” configurations is consistent with experimental evidence of a Cu/In proximity without complete alloying nor “burying” of the Cu, as suggested by the absence of an apparent shift of the XRD peaks after addition of In (Fig. 3) and N_2O titrations (Table 2). It is also consistent with the homogeneous dispersion of In and a strong binding with the Cu/SiO_2 catalyst. It is finally consistent with the reduction in nanoparticle size brought about by In doping (see Table 2 and the discussion in Section 3.2), since in our modeling the proposed InO_x buffer “necklace” structure mediates the interaction of Cu nanoparticles with the support and stabilizes small nanoparticles which therefore do not disaggregate turning into the not-easily-reduceable Cu species (presumably strongly interacting with the silica support) discussed in Section 3.3. We hypothesize that, reasonably, such not-easy-to-reduce Cu species do not play a catalytic role, and

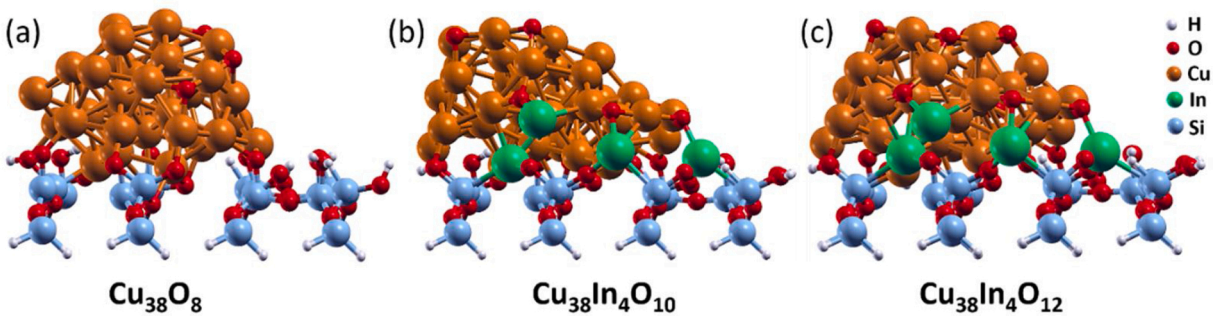

Fig. 7. Atomistic pictures of optimized lowest-energy putative global minimum structures of: (a) $Cu_{38}O_8$, (b) $Cu_{38}In_4O_{10}$ and (c) $Cu_{38}In_4O_{12}$ cluster catalysts deposited on a partially hydroxylated SiO_2 (100) surface.

we do not try to model them, but rather assume that Cu is mostly reduced to a metallic state. Note that in the GO sampling both In and Cu are unconstrained and free to interact with the oxygen atoms and the support. As a second main outcome of the GO search we derive that In atoms have more oxygen neighbors than Cu atoms, i.e., a stronger propensity of In to bind to O with respect to Cu, in tune with its stronger oxygen affinity. A Lowdin charge analysis reveals that In atoms are positively charged by about +0.7 *e*, with a significant charge transfer from In especially to the surrounding O atoms that are negatively charged with an average value of −0.41 *e* for $Cu_{38}In_4O_{10}/SiO_2$ and −0.42 *e* for $Cu_{38}In_4O_{12}/SiO_2$ catalysts. In atoms form strong chemical bonds with the neighboring Cu and O atoms (from both the support and on the cluster) with average In-Cu and In-O distances of about 2.85 Å and 2.12 Å. In short, In atoms are appreciably oxidized and are stabilized at the interface by the strong interaction with Cu on one side and SiO_2 on the other side. Also, we note that the the average oxygen-coordination of Cu in $Cu_{38}In_4O_{10}/SiO_2$ is closer to that in $Cu_{38}O_8/SiO_2$ with rerspect to $Cu_{38}In_4O_{12}/SiO_2$, so that in the following we will focus on the $Cu_{38}In_4O_{10}/SiO_2$ cluster as a model of the Cu-1In/SiO_2 catalyst.

To further characterize the electronic structure of our cluster models, we evaluated the Core-Level Shift (CLS) of Cu atoms in $Cu_{38}O_8/SiO_2$ and $Cu_{38}In_4O_{10}/SiO_2$, and we report them in Table S4. The average CLS of the Cu atoms in $Cu_{38}O_8$ is calculated to be 938.16 eV, and is greater than the average CLS of Cu in $Cu_{38}In_4O_{10}$ (938.06 eV) by +0.10 eV. The decrease of the calculated CLS in the In-doped catalyst is consistent with the experimentally observed CLS in Figs. S4–S6 in which the CLS of pure Cu is higher than Cu-In catalyst by +0.3 eV. This confirms that Cu in $Cu_{38}In_4O_{10}$ is less oxidized than in pure Cu system due to the presense of the InO_x interfacial phase. Overall, In acts as an electron donor and donates electrons to Cu in the Cu/SiO_2 catalyst. We also evaluated the CLS of In atoms, but these are less informative, as the difference between CLS of metallic and oxidic In phases is not large enough to allow for an unanmbiguous interpretation.

We then investigated the activation and evolution mechanism of H_2 on $Cu_{38}O_8/SiO_2$ and $Cu_{38}In_4O_{10}/SiO_2$ catalysts to help interpret and understand the catalytic activity toward H_2 production. We start from a key observation in Fig. 6 that the Cu-1In/SiO_2 catalyst presents a well-formed and narrow H_2O-TPD peak at a temperature of 400 °C, a temperature about 100 °C lower than that of the main H_2O-TPD peak at 500 °C that is present in both pure and doped catalysts. Note that in Fig. 6 we monitored the mass signal of H_2, so that the TPD reaction of Fig. 6 actually corresponds to H_2O dissociation and consequent H_2 evolution. We hypothesize that H_2O dissociation leading to H_2 evolution is a meaningful descriptor of the H_2 production ability of the given catalyst, as also suggested in Ref. [7] for Pt catalysts, and in the following we investigate such reaction on our cluster models.

The H_2O dissociation reaction proceeds through two consecutive steps: (i) adsorption and dissociation of H_2O to produce H* and OH* intermediates, followed by (ii) the activation of the O—H bond of the OH* intermediate to fully dissociate H atoms that can migrate on $Cu_{38}O_8/SiO_2$ and $Cu_{38}In_4O_{10}/SiO_2$ catalysts and recombine to produce H_2. Before moving to full reaction profile, it is worthwhile to examine the optimal configurations of H_2O adsorption in detail. We performed an extensive search to determine most preferable adsorption positions of H_2O molecules on $Cu_{38}O_8/SiO_2$ and $Cu_{38}In_4O_{10}/SiO_2$ catalysts. H_2O can be adsorbed on metal clusters in either a O-binding or a H-binding mode of adsorption, i.e., with wither O or H atoms closer to the cluster. We assumed as initial trial configurations (then confirmed by actual optimizations) that H_2O binds to metal Cu or In atoms in the O-binding mode, whereas it binds to O atoms of the catalysts in the H-binding mode (i.e., via hydrogen bonds). To accelerate this search, we started from the cluster structures generated by the GO algorithm, added a full layer of adsorbed H_2O molecules around the clusters, relaxed the geometry of the resulting complex, and then individually erased all H_2O molecules except one at a time and re-optimized the geometry to explore quickly a large variety of adsorption sites. Fig. 8 illustrates optimized structures of H_2O adsorption on the most stable sites of $Cu_{38}O_8/SiO_2$ and $Cu_{38}In_4O_{10}/SiO_2$ catalysts. The highest adsorption energy is naturally achieved when H_2O adsorbs over a metal atom simultaneously forming a hydrogen bond with the neighboring O atom (H-binding plus O-binding modes) with an adsorption energy of −0.65 eV and −0.57 eV for $Cu_{38}O_8/SiO_2$ and $Cu_{38}In_4O_{10}/SiO_2$, respectively. The adsorption energy of H_2O at the Cu metal site with a pure O-binding mode is −0.52 and −0.41 eV for $Cu_{38}O_8/SiO_2$ and $Cu_{38}In_4O_{10}/SiO_2$, respectively. Note that the adsorption energy of H_2O on $Cu_{38}O_8/SiO_2$ is a little higher than that on $Cu_{38}In_4O_{10}/SiO_2$. The geometry parameters of adsorbed H_2O are in line with these energies: For example, at "Cu and O" site on $Cu_{38}O_8/SiO_2$, the O···H hydrogen bond has a distance of 1.58 Å, which is shorter than that on $Cu_{38}In_4O_{10}/SiO_2$ (1.80 Å). One can also observe that the H_2O angle in adsorbed H_2O increases from 104.23° to 107.09° and one of the O—H bonds is slightly lengthened from 0.97 Å to 1.04 Å (as compared to a free H_2O molecule), indicating that the H_2O is activated at this primary step of adsorption.

The H_2O adsorption at most preferable sites were then chosen to investigate the full H_2O dissociation reaction pathway. Fig. 9 illustrates schematically the mechanistic steps and reaction energy profile of H_2O dissociation to produce 2 H* and 1 O* species on $Cu_{38}O_8/SiO_2$ and $Cu_{38}In_4O_{10}/SiO_2$ in the four cases here investigated, while the corresponding atomistic pictures of the structures on $Cu_{38}O_8/SiO_2$ at the "Cu and O" site are shown in Fig. 10 (the configurations of the corresponding intermediate states for all cases are displayed in Figs. S7–S9). Note that we ignore direct H_2O dissociation at In sites as it is not catalytically relevant: Briefly, H_2O adsorbs too strongly on the InO_x interfacial phase, increasing O—H dissociation barriers and therefore hindering H_2 evolution. The initial activation of H_2O involves direct dissociation of the H—O bond with one of its H atoms pointing towards either Cu or O atoms of the catalyst.

For H_2O dissociation at the Cu site, H_2O is directly dissociated on the Cu atom then proceeds through a transition state in which O—H breaking and H—Cu-forming bond concur. This first step requires overcoming a barrier of 1.53 eV and 1.23 eV for $Cu_{38}O_8/SiO_2$ and $Cu_{38}In_4O_{10}/SiO_2$, respectively. At variance with the Cu site, H_2O adsorbs on "Cu and O" site and then easily dissociates between the Cu and O atoms of the catalyst forming 2OH* species with small energy barrier (E_a) of 0.10 eV and 0.38 eV for the $Cu_{38}O_8$ and $Cu_{38}In_4O_{10}$, respectively. This first step is obviously easier on the "Cu and O" site than that on Cu site due to the strong hydrogen bond between H of the H_2O molecule and the O adatom of the catalyst. In the next step, the adsorbed hydroxyl *OH can undergo direct dissociation to produce a second H* adatom and one O* species. Looking at the optimized transition state structures (Figs. S5–S7 and 10), the O—H bond of *OH is lengthened and the H—Cu bond which is forming is shortened as compared with the *OH intermediate. On $Cu_{38}O_8/SiO_2$, this OH dissociation requires overcoming an energy barrier of 1.65 eV at the "Cu" site, and 1.85 eV at the "Cu and O" site, respectively, while on $Cu_{38}In_4O_{10}/SiO_2$ the E_a for OH dissociation is 1.88, eV at the "Cu" site, and 1.22 eV at the "Cu and O" site, respectively (Fig. 9). We can therefore conclude that: (i) the OH dissociation is the rate determining step (RDS) for H_2O dissociation (which is reasonable due to the stronger O—H bond in the hydroxyl with respect to H_2O), and (ii) the bimetallic $Cu_{38}In_4O_{10}/SiO_2$ catalyst has a better performance than $Cu_{38}O_8$ catalyst due to a smaller RDS barrier. Looking at the transition state structures and the weak correlation with other descriptors we argue that the decreased barriers to H_2 evolution can be attributed to an increased structural fluxionality of the Cu cluster in the presence of In (see the SI). Note that full H_2O dissociation (including *OH dissociation) is needed for H_2 evolution, as it is obvious from the energy profile of Fig. 9, in which the "*H + *OH" configurations always represent the resting states. Roughly, we can calculate an *average* barrier for *OH dissociation to be 1.765 eV and 1.525 eV for $Cu_{38}O_8/SiO_2$ and $Cu_{38}In_4O_{10}/SiO_2$, respectively.

Comparing to experimental results, the Cu-1In/SiO_2 H_2O-TPD plot in Fig. 6 shows two different peaks at temperatures around 673 K and 773

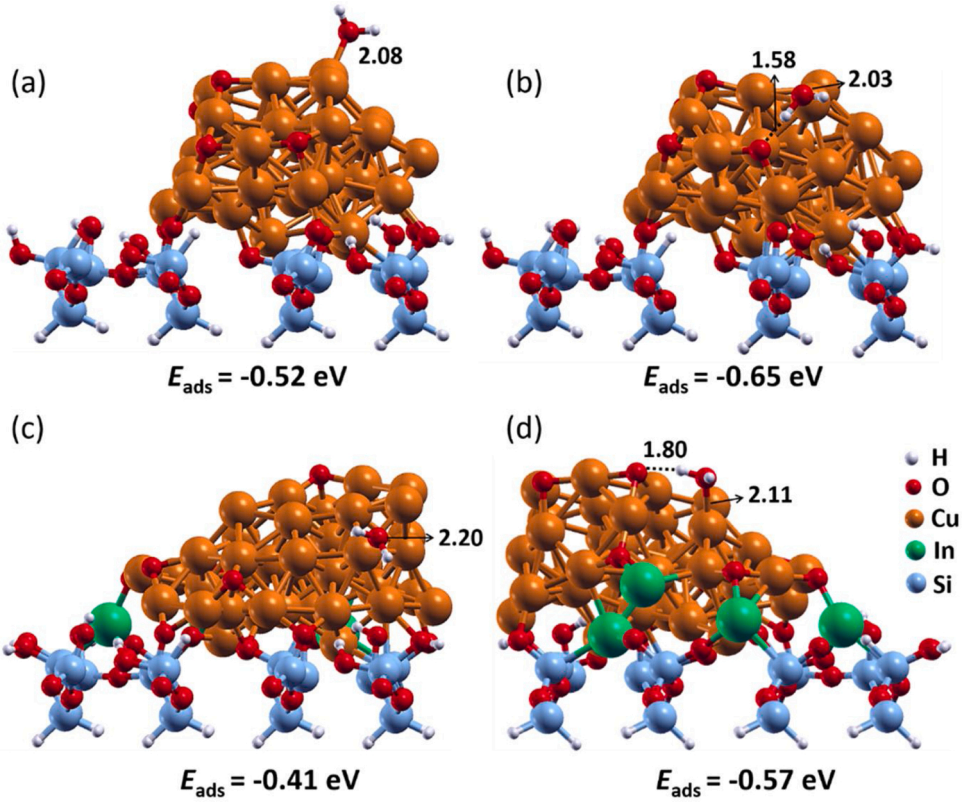

Fig. 8. Atomistic pictures of H_2O molecules positioned on preferred adsorption sites on (a,b) $Cu_{38}O_8/SiO_2$ and (c,d) $Cu_{38}In_4O_{10}/SiO_2$ catalysts, in either (a,c) O-binding or (bd,) H-binding modes. Adsorption energies in eV are reported as E_{ads} values. Selected interatomic distances are also reported.

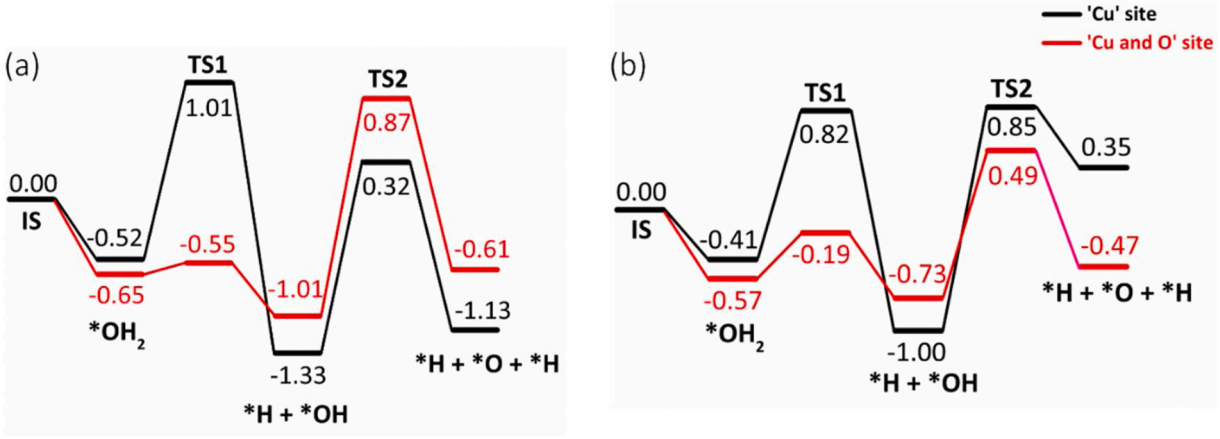

Fig. 9. Schematic energy profiles for H_2O dissociation to produce 2 H* and 1 O* products on (a) $Cu_{38}O_8/SiO_2$, and (b) $Cu_{38}O_8/SiO_2$ and $Cu_{38}In_4O_{10}/SiO_2$ catalysts.

K, whereas in Cu/SiO_2 H_2O-TPD plot only one peak appears at 773 K. Estimating the corresponding energy barriers via the Arrhenius equation: k = A exp (E_a/RT), where A is the Arrhenius prefactor (the frequency factor), R is the universal gas constant, T is the temperature (in K) and E_a is the energy barrier, and assuming for definiteness a turnover-frequency (TOF) of 4.2 s^{-1} and an Arrhenius prefactor A = 1 × 10^{13}, our estimate for the experimental barrier is ≈1.65 eV for the peak at 673 K, and ≈1.90 eV for the peak at 773 K, respectively. The order of magnitude of the experimentally estimated barriers for the main H_2O-TPD peak is thus close to the larger energy barriers predicted from theory (1.88 eV for "Cu and O" site on $Cu_{38}O_8/SiO_2$ and 1.85 eV for "Cu" site on $Cu_{38}In_4O_{10}/SiO_2$). Moreover, in agreement with the experiments, theory predicts that on the bimetallic Cu-In catalyst energy barriers exist appreciably lower than those on pure Cu, although the theoretically predicted decrease (around 0.4 eV, i.e., from 1.65 eV for "Cu" site on $Cu_{38}O_8/SiO_2$ to 1.22 eV for "Cu and O" site on $Cu_{38}In_4O_{10}/SiO_2$) is larger than that estimated from experimental H_2O-TPD plot (0.25 eV, from 1.90 eV to 1.65 eV).

In summary, DFT calculations confirm that the electronic properties of Cu atoms in Cu/SiO_2 are influenced by the presence of In, as evidenced by the CLS and Lowdin charge analysis: In acts as an electron donor and donates electron charge to Cu. The bimetallic Cu-In catalyst model also exhibits a superior catalytic activity for the direct dissociation of H_2O to H* and O* products with smaller energy barriers, in good agreement with and rationalizing experimental H_2O-TPD data. Taking then H_2O dissociation as a good descriptor of H_2 evolution, the conclusion that In-doping can enhance catalytic H_2 production of Cu catalysts, and that Cu-1In is superior to pure Cu, is supported and

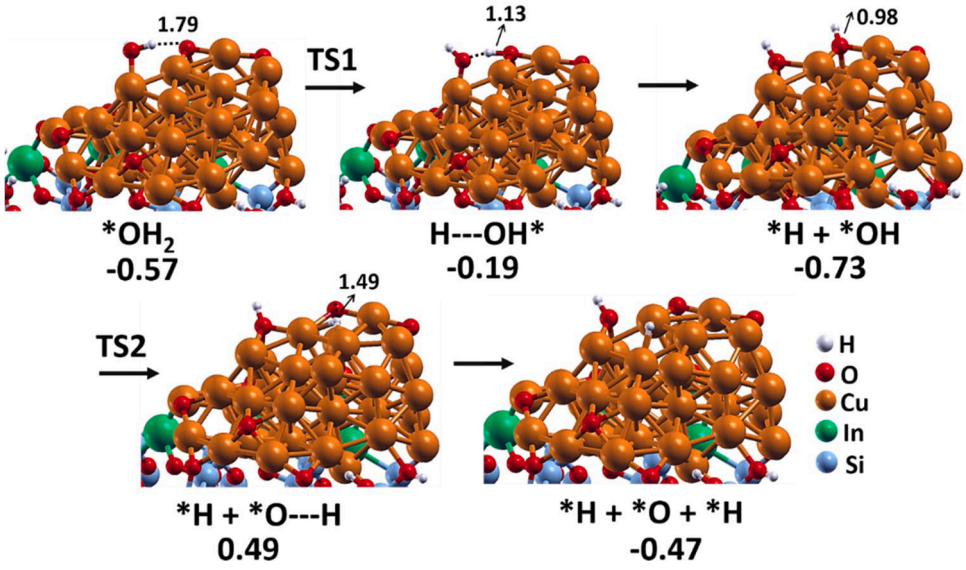

Fig. 10. Schematic atomistic depiction of the full reaction pathway for H_2O dissociation to *H + O* + H* on $Cu_{38}In_4O_{10}/SiO_2$ at the "Cu and O" site.

rationalized by our DFT modeling.

4. Conclusions

With this work we demonstrated that the potentiality of In in heterogeneous catalysis can be extended to the promotion of the H_2 selectivity and productivity during MSR reaction by influencing the structure and electronics of Cu nanoparticles.

To this purpose, a series of In-modified catalysts were synthetized via a urea-assisted co-precipitation method resulting in Cu-In/SiO_2 bimetallic catalysts with homogeneously dispersed InO_x phase in tight interaction with small Cu nanoparticles (2.6 nm). The catalytic activity tests showed that just 1 wt.% of In promotes the reaction by producing an almost stoichiometric H_2/CO_2 stream already at reaction temperatures as low as 220 °C. For comparison, at the same conditions, the Cu/SiO_2 catalysts exhibited a lower H_2 selectivity, a H_2/CO_2 ratio of 2.76 mol/mol, and in turn lower H_2 productivity.

Via a series of characterization tools, i.e., XPS XRD, N_2O titrations, TPR analyses with H_2 and CO, and CH_3OH- and H_2O-TPD, supported by computational modeling correlating H_2 selectivity with the novel H_2O-TPD peak observed in experiment for the Cu-In/SiO_2 catalyst, we rationalized that the enhanced H_2 selectivity is due to an enrichment of electron density of the Cu nanoparticles in the presence of In, in tune with theoretical-suggested structural phenomena, that is, the formation of InO_x "necklace" buffer phases at the interface between the Cu nanoparticles and the silica support and an enhanced fluxionality of the catalysts. Interestingly, the higher the In content, the higher this electron enrichment. However, too much In (as in the 5 wt.% trials) leads to covering the surface of the Cu with InO_x species thus ultimately deactivating the catalyst. The opposite promoting and detrimental effects of In must therefore be carefully balanced in order to obtain the desired overall positive effect on the H_2 production.

This work provides a clear evidence of how In acts as H_2 production booster for Cu catalysts in MSR, paving the way to even more active catalytic materials. Building on our previous research on Cu-based catalysts for the MSR reaction [21], we showed how strong the impact of the structure and electronics of Cu nanoparticles in the range of 2–3 nm is on the catalytic activity and how that is a potent tool to increase the H_2 productivity.

CRediT authorship contribution statement

Filippo Bossola: Conceptualization, Validation, Formal analysis, Investigation, Resources, Data curation, Writing - original draft, Visualization, Writing - review & editing. **Thantip Roongcharoen:** Investigation, Formal analysis, Visualization, Writing - original draft. **Mauro Coduri:** Investigation, Visualization, Formal analysis, Writing - original draft. **Claudio Evangelisti:** Investigation, Visualization, Writing - original draft. **Ferenc Somodi:** Investigation, Formal analysis, Writing - original draft, Visualization. **Luca Sementa:** Software, Resources, Investigation. **Alessandro Fortunelli:** Methodology, Formal analysis, Supervision. **Vladimiro Dal Santo:** Supervision, Project administration, Funding acquisition.

Declaration of Competing Interest

The authors declare that they have no known competing financial interests or personal relationships that could have appeared to influence the work reported in this paper.

Acknowledgments

The authors thank the financial support through BIKE project, this project has received funding from the European Union's Horizon 2020 research and innovation program under the Marie Skłodowska-Curie grant agreement N° 813748. The authors also thank Miklós Németh of Centre for Energy Research, Budapest, for his precious contribution with the XPS analyses.

Appendix A. Supplementary data

Supplementary material related to this article can be found, in the online version, at doi:https://doi.org/10.1016/j.apcatb.2021.120398.

References

[1] A. Gervasini, J.A. Perdigon-Melon, C. Guimon, A. Auroux, An in-depth study of supported In_2O_3 catalysts for the selective catalytic reduction of NOx: the influence of the oxide support, J. Phys. Chem. B 110 (2006) 240–249.
[2] H. Berndt, F.W. Schütze, M. Richter, T. Sowade, W. Grünert, Selective catalytic reduction of NO under lean conditions by methane and propane over indium/cerium-promoted zeolites, Appl. Catal. B: Environ. 40 (2003) 51–67.
[3] H. Lorenz, W. Jochum, B. Klötzer, M. Stöger-Pollach, S. Schwarz, K. Pfaller, S. Penner, Novel methanol steam reforming activity and selectivity of pure In2O3, Appl. Catal. A Gen. 347 (2008) 34–42.

[4] O. Martin, A.J. Martín, C. Mondelli, S. Mitchell, T.F. Segawa, R. Hauert, C. Drouilly, D. Curulla-Ferré, J. Pérez-Ramírez, Indium oxide as a superior catalyst for methanol synthesis by CO_2 hydrogenation, Angew. Chem. Int. Ed. 55 (2016) 6261–6265.

[5] J. Wang, H. Wang, P. Hu, Theoretical insight into methanol steam reforming on indium oxide with different coordination environments, Sci. China Chem. 61 (2018) 336–343.

[6] K. Ploner, L. Schlicker, A. Gili, A. Gurlo, A. Doran, L. Zhang, M. Armbrüster, D. Obendorf, J. Bernardi, B. Klötzer, S. Penner, Reactive metal-support interaction in the Cu-In_2O_3 system: intermetallic compound formation and its consequences for CO_2-selective methanol steam reforming, Sci. Technol. Adv. Mater. 20 (2019) 356–366.

[7] D. Liu, Y. Men, J. Wang, G. Kolb, X. Liu, Y. Wang, Q. Sun, Highly active and durable Pt/In_2O_3/Al_2O_3 catalysts in methanol steam reforming, Int. J. Hydrogen Energy 41 (2016) 21990–21999.

[8] X. Liu, Y. Men, J. Wang, R. He, Y. Wang, Remarkable support effect on the reactivity of Pt/In_2O_3/MO_x catalysts for methanol steam reforming, J. Power Sources 364 (2017) 341–350.

[9] R.L. Barbosa, V. Papaefthimiou, Y.T. Law, D. Teschner, M. Hävecker, A. Knop-Gericke, R. Zapf, G. Kolb, R. Schlögl, S. Zafeiratos, Methanol steam reforming over indium-promoted Pt/Al_2O_3 catalyst: nature of the active surface, J. Phys. Chem. C 117 (2013) 6143–6150.

[10] G. Kolb, S. Keller, D. Tiemann, K.P. Schelhaas, J. Schürer, O. Wiborg, Design and operation of a compact microchannel 5$kW_{el,net}$ methanol steam reformer with novel Pt/In_2O_3 catalyst for fuel cell applications, Chem. Eng. J. 207–208 (2012) 388–402.

[11] H. Lorenz, S. Turner, O.I. Lebedev, G. Van Tendeloo, B. Klötzer, C. Rameshan, K. Pfaller, S. Penner, Pd-In_2O_3 interaction due to reduction in hydrogen: consequences for methanol steam reforming, Appl. Catal. A Gen. 374 (2010) 180–188.

[12] Y. Men, G. Kolb, R. Zapf, M. O'Connell, A. Ziogas, Methanol steam reforming over bimetallic Pd-In/Al_2O_3 catalysts in a microstructured reactor, Appl. Catal. A Gen. 380 (2010) 15–20.

[13] M. Neumann, D. Teschner, A. Knop-Gericke, W. Reschetilowski, M. Armbrüster, Controlled synthesis and catalytic properties of supported In-Pd intermetallic compounds, J. Catal. 340 (2016) 49–59.

[14] P. Sun, G. Siddiqi, W.C. Vining, M. Chi, A.T. Bell, Novel Pt/Mg(In)(Al)O catalysts for ethane and propane dehydrogenation, J. Catal. 282 (2011) 165–174.

[15] D. Li, X. Li, J. Gong, Catalytic reforming of oxygenates: state of the art and future prospects, Chem. Rev. 116 (2016) 11529–11653.

[16] S. Sá, H. Silva, L. Brandão, J.M. Sousa, A. Mendes, Catalysts for methanol steam reforming-A review, Appl. Catal. B: Environ. 99 (2010) 43–57.

[17] N. Scotti, F. Bossola, F. Zaccheria, N. Ravasio, Copper–zirconia catalysts: powerful multifunctional catalytic tools to approach sustainable processes, Catalysts 10 (2020) 168.

[18] Y. Matsumura, H. Ishibe, Durable copper-zinc catalysts modified with indium oxide in high temperature steam reforming of methanol for hydrogen production, J. Power Sources 209 (2012) 72–80.

[19] A.A. Lytkina, N.A. Zhilyaeva, M.M. Ermilova, N.V. Orekhova, A.B. Yaroslavtsev, Influence of the support structure and composition of Ni-Cu-based catalysts on hydrogen production by methanol steam reforming, Int. J. Hydrogen Energy 40 (2015) 9677–9684.

[20] L. Mayr, B. Klötzer, D. Zemlyanov, S. Penner, Steering of methanol reforming selectivity by zirconia-copper interaction, J. Catal. 321 (2015) 123–132.

[21] F. Bossola, N. Scotti, F. Somodi, M. Coduri, C. Evangelisti, V. Dal Santo, Electron-poor copper nanoparticles over amorphous zirconia-silica as all-in-one catalytic sites for the methanol steam reforming, Appl. Catal. B: Environ. 258 (2019), 118016.

[22] D. Das, J. Llorca, M. Dominguez, S. Colussi, A. Trovarelli, A. Gayen, Methanol steam reforming behavior of copper impregnated over CeO_2-ZrO_2 derived from a surfactant assisted coprecipitation route, Int. J. Hydrogen Energy 40 (2015) 10463–10479.

[23] Y. Matsumura, H. Ishibe, Suppression of CO by-production in steam reforming of methanol by addition of zinc oxide to silica-supported copper catalyst, J. Catal. 268 (2009) 282–289.

[24] Z. Wang, W. Wang, G. Lu, Studies on the active species and on dispersion of Cu in Cu/SiO_2 and Cu/Zn/SiO_2 for hydrogen production via methanol partial oxidation, Int. J. Hydrogen Energy 28 (2003) 151–158.

[25] J. Károlyi, M. Németh, C. Evangelisti, G. Sáfrán, Z. Schay, A. Horváth, F. Somodi, Carbon dioxide reforming of methane over Ni–In/SiO_2 catalyst without coke formation, J. Ind. Eng. Chem. 58 (2018) 189–201.

[26] Z.Q. Wang, Z.N. Xu, S.Y. Peng, M.J. Zhang, G. Lu, Q.S. Chen, Y. Chen, G.C. Guo, High-performance and long-lived Cu/SiO_2 nanocatalyst for CO_2 hydrogenation, ACS Catal. 5 (2015) 4255–4259.

[27] V. Dal Santo, C. Dossi, A. Fusi, R. Psaro, C. Mondelli, S. Recchia, Fast transient infrared studies in material science: development of a novel low dead-volume, high temperature DRIFTS cell, Talanta 66 (2005) 674–682.

[28] T. Roisnel, J. Rodríguez-Carvajal, WinPLOTR: A windows tool for powder diffraction pattern analysis, Mater. Sci. Forum. 378–381 (2001) 118–123.

[29] A. Gallo, C. Pirovano, M. Marelli, R. Psaro, V. Dal Santo, Hydrogen production by glycerol steam reforming with Ru-based catalysts: a study on Sn doping, Chem. Vap. Depos. 16 (2010) 305–310.

[30] D.J. Wales, J.P.K. Doye, Global optimization by basin-hopping and the lowest energy structures of Lennard-Jones clusters containing up to 110 atoms, J. Phys. Chem. A 101 (1997) 5111–5116.

[31] N. Metropolis, A.W. Rosenbluth, M.N. Rosenbluth, A.H. Teller, E. Teller, Equation of state calculations by fast computing machines, J. Chem. Phys. 21 (1953) 1087–1092.

[32] Openmx, (n.d.). http://www.openmx-square.org/.

[33] T. Ozaki, H. Kino, Numerical atomic basis orbitals from H to Kr, Phys. Rev. B - Condens. Matter Mater. Phys. 69 (2004) 1–19.

[34] T.V.T. Duy, T. Ozaki, A decomposition method with minimum communication amount for parallelization of multi-dimensional FFTs, Comput. Phys. Commun. 185 (2014) 153–164.

[35] J.P. Perdew, K. Burke, M. Ernzerhof, Generalized gradient approximation made simple, Phys. Rev. Lett. 77 (1996) 3865–3868.

[36] OpenmxData, (n.d.). https://t-ozaki.issp.u-tokyo.ac.jp/vps_pao2019.

[37] P. Giannozzi, S. Baroni, N. Bonini, M. Calandra, R. Car, C. Cavazzoni, D. Ceresoli, G.L. Chiarotti, M. Cococcioni, I. Dabo, A. Dal Corso, S. De Gironcoli, S. Fabris, G. Fratesi, R. Gebauer, U. Gerstmann, C. Gougoussis, A. Kokalj, M. Lazzeri, L. Martin-Samos, N. Marzari, F. Mauri, R. Mazzarello, S. Paolini, A. Pasquarello, L. Paulatto, C. Sbraccia, S. Scandolo, G. Sclauzero, A.P. Seitsonen, A. Smogunov, P. Umari, R.M. Wentzcovitch, QUANTUM ESPRESSO: a modular and open-source software project for quantum simulations of materials, J. Phys. Condens. Matter 21 (2009).

[38] P. Gianozzi, O. Andreussi, T. Brumme, O. Bunau, M. Buongiorno Nardelli, M. Calandra, R. Car, C. Cavazzoni, D. Ceresoli, M. Cococcioni, N. Colonna, I. Carnimeo, A. Dal Corso, S. de Gironcoli, P. Delugas, R.A. Di Stasio Jr., A. Ferretti, A. Floris, G. Fratesi, G. Fugallo, R. Gebauer, U. Gerstmann, F. Giustino, T. Gorni, J. Jia, M. Kawamura, H.-Y. Ko, A. Kokalj, E. Kucukbenli, M. Lazzero, M. Marsili, N. Marzari, F. Mauri, N.L. Nguyen, H.-V. Nguyen, A. Orero-de-la-Roza, L. Paulatto, S. Poncé, D. Rocca, R. Sabatini, B. Santra, M. Schlipf, A.P. Seitsonen, A. Smugunov, I. Timrov, T. Thonhauser, P. Umari, N. Vast, X. Wu, S. Baroni, Advanced capabilities for materials modelling with Quantum ESPRESSO, J. Phys. Condens. Matter 29 (2017), 465901.

[39] K.F. Garrity, J.W. Bennett, K.M. Rabe, D. Vanderbilt, Pseudopotentials for high-throughput DFT calculations, Comput. Mater. Sci. 81 (2014) 446–452.

[40] G. Henkelman, H. Jónsson, Improved tangent estimate in the nudged elastic band method for finding minimum energy paths and saddle points, J. Chem. Phys. 113 (2000) 9978–9985.

[41] G. Henkelman, B.P. Uberuaga, H. Jónsson, Climbing image nudged elastic band method for finding saddle points and minimum energy paths, J. Chem. Phys. 113 (2000) 9901–9904.

[42] P.O. Löwdin, On the non-orthogonality problem connected with the use of atomic wave functions in the theory of molecules and crystals, J. Chem. Phys. 18 (1950) 365–375.

[43] E. Pehlke, M. Scheffler, Evidence for site-sensitive screening of core holes at the Si and Ge (001) surface, Phys. Rev. Lett. 71 (1993) 2338–2341.

[44] J.P. Espinós, J. Morales, A. Barranco, A. Caballero, J.P. Holgado, A.R. González-Elipe, Interface effects for Cu, CuO, and Cu_2O deposited on SiO_2 and ZrO_2. XPS determination of the valence state of copper in Cu/SiO_2 and Cu/ZrO_2 catalysts, J. Phys. Chem. B 106 (2002) 6921–6929.

[45] T. Tsoncheva, V. Dal Santo, A. Gallo, N. Scotti, M. Dimitrov, D. Kovacheva, Structure and catalytic activity of hosted in mesoporous silicas copper species: Effect of preparation procedure and support pore topology, Appl. Catal. A Gen. 406 (2011) 13–21.

[46] V.G. Deshmane, R.Y. Abrokwah, D. Kuila, Synthesis of stable Cu-MCM-41 nanocatalysts for H_2 production with high selectivity via steam reforming of methanol, Int. J. Hydrogen Energy 40 (2015) 10439–10452.

[47] G. Onyestyák, S. Harnos, D. Kalló, Indium, as an efficient co-catalyst of Cu/ Al_2O_3 in the selective hydrogenation of biomass derived fatty acids to alcohols, Catal. Commun. 26 (2012) 19–24.

[48] D. Kim, N. Becknell, Y. Yu, P. Yang, Room-temperature dynamics of vanishing copper nanoparticles supported on silica, Nano Lett. 17 (2017) 2732–2737.

[49] H. Yue, Y. Zhao, S. Zhao, B. Wang, X. Ma, J. Gong, A copper-phyllosilicate core-sheath nanoreactor for carbon-oxygen hydrogenolysis reactions, Nat. Commun. 4 (2013) 1–7.

[50] H. Yang, Y. Chen, X. Cui, G. Wang, Y. Cen, T. Deng, W. Yan, J. Gao, S. Zhu, U. Olsbye, J. Wang, W. Fan, A highly stable copper-based catalyst for clarifying the catalytic roles of Cu° and Cu^{+} species in methanol dehydrogenation, Angew. Chem. 130 (2018) 1854–1858.

[51] X.M. Zhang, P. Tian, W. Tu, Z. Zhang, J. Xu, Y.F. Han, Tuning the dynamic interfacial structure of copper-ceria catalysts by indium oxide during CO oxidation, ACS Catal. 8 (2018) 5261–5275.

[52] R.X. Zhou, X.Y. Jiang, J.X. Mao, X.M. Zheng, Oxidation of carbon monoxide catalyzed by copper-zirconium composite oxides, Appl. Catal. A Gen. 162 (1997) 213–222.

[53] N. Scotti, M. Dangate, A. Gervasini, C. Evangelisti, N. Ravasio, F. Zaccheria, Unraveling the role of low coordination sites in a cu metal nanoparticle: a step toward the selective synthesis of second generation biofuels, ACS Catal. 4 (2014).

[54] K. Samson, M. Sliwa, R.P. Socha, K. Góra-Marek, D. Mucha, D. Rutkowska-Zbik, J. F. Paul, M. Ruggiero-Mikoajczyk, R. Grabowski, J. Soczyński, Influence of ZrO_2 structure and copper electronic state on activity of Cu/ZrO_2 catalysts in methanol synthesis from CO_2, ACS Catal. 4 (2014) 3730–3741.

[55] G. Moretti, A. Palma, E. Paparazzo, M. Satta, Auger parameter and Wagner plot studies of small copper clusters, Surf. Sci. 646 (2016) 298–305.

[56] A.M. Venezia, X-ray photoelectron spectroscopy (XPS) for catalysts characterization, Catal. Today 77 (2003) 359–370.

[57] M. Faur, M. Faur, D.T. Jayne, M. Goradia, C. Goradia, XPS investigation of anodic oxides grown on p-type InP, Surf. Interface Anal. 15 (1990) 641–650.

[58] X. Liu,, W.-Z. Lang, L.-L. Long, C.-L. Hu, L.-F. Chu, Y.-J. Guo, Improved catalytic performance in propane dehydrogenation of PtSn/c-Al2O3 catalysts by doping indium, Chem. Eng. J. 247 (2014) 183–192, https://doi.org/10.1016/j.cej.2014.02.084.

[59] B. Frank, F.C. Jentoft, H. Soerijanto, J. Kröhnert, R. Schlögl, R. Schomäcker, Steam reforming of methanol over copper-containing catalysts: influence of support material on microkinetics, J. Catal. 246 (2007) 177–192.

[60] L.C. Wang, Q. Liu, M. Chen, Y.M. Liu, Y. Cao, H.Y. He, K.N. Fan, Structural evolution and catalytic properties of nanostructured Cu/ZrO_2 catalysts prepared by oxalate gel-coprecipitation technique, J. Phys. Chem. C 111 (2007) 16549–16557.

[61] J. Gong, H. Yue, Y. Zhao, S. Zhao, L. Zhao, J. Lv, S. Wang, X. Ma, Synthesis of ethanol via syngas on Cu/SiO 2 catalysts with balanced Cu°-Cu^{+} sites, J. Am. Chem. Soc. 134 (2012) 13922–13925.

[62] C.Z. Yao, L.C. Wang, Y.M. Liu, G.S. Wu, Y. Cao, W.L. Dai, H.Y. He, K.N. Fan, Effect of preparation method on the hydrogen production from methanol steam reforming over binary Cu/ZrO_2 catalysts, Appl. Catal. A Gen. 297 (2006) 151–158.

[63] Y. Zhang, C. Ye, C. Guo, C. Gan, X. Tong, In_2O_3-modified Cu/SiO_2 as an active and stable catalyst for the hydrogenation of methyl acetate to ethanol, Cuihua Xuebao/Chin. J. Catal. 39 (2018) 99–108.

[64] X. He, Y. Wang, X. Zhang, M. Dong, G. Wang, B. Zhang, Y. Niu, S. Yao, X. He, H. Liu, Controllable in situ surface restructuring of Cu catalysts and remarkable enhancement of their catalytic activity, ACS Catal. 9 (2019) 2213–2221.

[65] D.A.J.M. Ligthart, R.A. Van Santen, E.J.M. Hensen, Influence of particle size on the activity and stability in steam methane reforming of supported Rh nanoparticles, J. Catal. 280 (2011) 206–220.

[66] A.M. Karim, C. Howard, B. Roberts, L. Kovarik, L. Zhang, D.L. King, Y. Wang, In situ X-ray absorption fine structure studies on the effect of pH on Pt electronic density during aqueous phase reforming of glycerol, ACS Catal. 2 (2012) 2387–2394.

[67] A.P. Tsai, S. Kameoka, K. Nozawa, M. Shimoda, Y. Ishii, Intermetallic: a pseudoelement for catalysis, Acc. Chem. Res. 50 (2017) 2879–2885.

[68] I. Ritzkopf, S. Vukojević, C. Weidenthaler, J.D. Grunwaldt, F. Schüth, Decreased CO production in methanol steam reforming over Cu/ZrO_2 catalysts prepared by the microemulsion technique, Appl. Catal. A Gen. 302 (2006) 215–223.